Spectrally resolved three-dimensional bioluminescence tomography with a level-set strategy

Kai Liu,[1,†] Xin Yang,[1,†] Dan Liu,[1] Chenghu Qin,[1] Junting Liu,[2] Zhijun Chang,[1] Min Xu,[1] and Jie Tian[1,2,*]

[1]*Medical Image Processing Group, Institute of Automation, Chinese Academy of Sciences,*
P.O. Box 2728, Beijing 100190, China
[2]*Life Science Center, Xidian University, Xian, Shaanxi 710071, China*
*Corresponding author: tian@ieee.org

A reconstruction method is presented for spectrally resolved three-dimensional bioluminescence tomography (BLT) in heterogeneous media using a level-set strategy. In order to reconstruct internal bioluminescent sources, a level-set strategy is utilized to quantitatively localize the distribution of bioluminescent sources. The results in numerical phantom experiments clearly show that the proposed method can tolerate different initial values and noise levels and, furthermore, can work credibly even when the number of phases (levels) is not known *a priori*. In addition, a mouse atlas reconstruction is employed to demonstrate the effectiveness of the proposed method in turbid mouse geometry. Finally, the physical experiment further evaluates the method's potential in practical applications. © 2010 Optical Society of America

OCIS codes: 170.6960, 100.3190, 170.3660, 170.6280.

1. INTRODUCTION

Bioluminescence imaging (BLI) makes it possible to elucidate cellular signatures to better understand the effects of human disease in small animal models *in vivo*. In recent years, BLI has given researchers insight into a wide variety of biomedical applications, such as gene expression, cell trafficking, transgene expression, and drug development and evaluation [1–5]. Since there is no inherent tissue autofluorescence generated by external illumination, the sensitivity of BLI is higher [6] than that of fluorescence molecular imaging (FMI). Furthermore, since BLI is semi-quantitative and has poor spatial resolution, bioluminescence tomography (BLT) provides unambiguous three-dimensional bioluminescent source information, which could further enhance applications in biomedicine.

In recent years, BLT has become a research hot spot, and many contributions have been made to the inverse problem [7–13]. Unlike high-energy particles used in computed tomography (CT), positron emission tomography (PET), or single photon emission computed tomography (SPECT), photons emitted from bioluminescent sources undergo multiple scattering and potential absorption in biological tissue [14]. This diffusive nature makes the inverse source problem highly ill-posed, non-unique, and noise-sensitive. While the uniqueness theorem for BLT has theoretically shown that a solution is not unique generally [15], in practice, incorporation of some kinds of *a priori* information can alleviate ill-posedness and strengthen solution uniqueness. The *a priori* information about the source-permissible region is commonly selected as the domain of interest (DOI), and many numerical methods [9,10,16,17] have verified the feasibility of BLT based on single spectral measurements. Since the spectral characteristics can offer more knowledge about the underlying bioluminescent sources, multispectral measurement is another kind of *a priori* information to further reduce the ill-posedness of the inverse problem compared with single spectral measurements. The methods based on multispectral information have demonstrated that the *a priori* knowledge can produce more valuable tomographic information [18–21]. By heating small volumes of interest to change the optical signal, the temperature-modulated multispectral method can further overcome the inherent challenges in BLT [22]. Furthermore,, based on the sparse characteristic of bioluminescent sources, the inverse problem regularized with both l_1 and total-variation norms have been also integrated to fully utilize sparse *a priori* knowledge about the distribution of bioluminescent sources [23]. Recently, a generalized-graph-cuts-based reconstruction method has been developed that is gradient-free and can remarkably improve the reconstruction efficiency [24].

In this paper, we propose a level-set-based reconstruction method for spectrally resolved three-dimensional BLT. In many of the existing methods, relatively small DOIs are apt to be adopted [9,10,16,17], which is not always reliable or feasible for defining such a region effectively. However, the proposed method requires much less *a priori* information about the source-permissible region to obtain feasible results. Moreover, it can adapt different initial values and can tolerate high experimental noise. The reconstruction on mouse atlas further demonstrates the potential in *in vivo* mouse applications. To the best of our knowledge, level set has not been applied in BLT. Osher and Sethian first proposed the level-set idea for

tracing interfaces between different phases of fluid flows [25]. The flexibility of the level set has made it possible to deal with dynamic evolutions and topological changes of curves and surfaces. Hence, the methods have been tremendously expanded in many fields over the past decades [26–30]. Furthermore, many numerical methods were successively developed to enhance the performance of level-set methods. A narrowband technique was proposed to improve the efficiency [31], and shock-capturing schemes for solving problems containing discontinuities were successfully developed to enhance the performance of level-set methods [32–34].

Being different from the standard level-set methods, the discontinuous level-set methods constitute an alternative[35,36]. In these methods, the curves dividing the whole domain into subdomains are defined by discontinuities in the level-set functions. One category of discontinuous methods, called the piecewise-constant level-set method, has been discussed in the application of image segmentation problems [37,38]. In contrast to other level-set formulations, it requires only one level-set function to identify an arbitrary number of phases [39], which makes it simpler and require less storage capacity. Lately, it has also been applied to inverse problems. Tai and Li [40] first used the level-set method to formulate the elliptic inverse problem in two-dimensional Cartesian grids. Li *et al.* [41] applied this method in reservoir description to identify the permeability field with zonation structure, also in two dimensions. In this contribution, based on the piecewise-constant level-set method, we try to reconstruct the bioluminescent source distribution in three dimensions.

The remainder of this paper is organized as follows. In the Section 2, the forward diffusion approximation model and the inverse problem for spectrally resolved BLT are introduced briefly. In Section 3, the level-set-based reconstruction method for BLT and related issues are presented. In Section 4, numerical phantom experiments first are compared with a gradient-based method to verify our proposed method with various initial values, noise levels, and more phases than one actually needs. Then a reconstruction using a mouse atlas demonstrates the feasibility of the proposed method in heterogeneous mouse geometry. Furthermore, taking advantage of the multispectral measurements from our optical imaging system, a physical experiment further evaluates its reliability. Finally, the conclusions are presented in Section 5.

2. FORMULATIONS OF SPECTRALLY RESOLVED BIOLUMINESCENCE TOMOGRAPHY

The process of photon propagation in biological tissue is governed by the radiative transfer equation (RTE) [42]. However, the RTE is computationally expensive. In bioluminescence imaging, photon scattering predominates over absorption in tissue of small animals in the red-light and near-infrared (NIR) spectral window, so the process can be modeled by the diffusion equation, which is basically a first-order spherical harmonic approximation of the RTE. It can be assumed that the bioluminescent sources in tissue are steady state, and the emission spec-

trum of sources can be divided into m spectrum bands. In the ϑth band, we have the diffusion equation [22,43]:

$$-\nabla \cdot (D_\vartheta(\mathbf{r}) \nabla (\Phi_\vartheta(\mathbf{r})\,)) + \mu_{a,\vartheta}(\mathbf{r})\Phi_\vartheta(\mathbf{r}) = q_\vartheta(\mathbf{r}) \quad (\mathbf{r} \in \Omega).$$
(1)

In the bioluminescence imaging experiments, assuming that the whole process is performed in a totally dark environment and that there is no external photon transport into Ω through its boundary $\partial\Omega$ in the corresponding spectral band, we have the Robin boundary condition [22]:

$$\Phi_\vartheta(\mathbf{r}) + 2A(\mathbf{r};n,n')D_\vartheta(\mathbf{r})(v(\mathbf{r}) \cdot \nabla\Phi_\vartheta(\mathbf{r})) = 0 \quad (\mathbf{r} \in \partial\Omega),$$
(2)

where Ω and $\partial\Omega$ denote the domain and the boundary of the domain, respectively, $D_\vartheta(\mathbf{r})$ the exiting flux density at location $\mathbf{r}$ in the ϑth band, $q_\vartheta(\mathbf{r})$ the source distribution, $\mu_{a,\vartheta}(\mathbf{r})$ the absorption coefficient, $\mu_{s,\vartheta}(\mathbf{r})$ the scattering coefficient, $D_\vartheta(\mathbf{r}) = 1/(3(\mu_{a,\vartheta}(\mathbf{r}) + (1-g)\mu_{s,\vartheta}(\mathbf{r}))$ the optical diffusion coefficient, g the anisotropy parameter, and $v(\mathbf{r})$ the unit outer normal on $\partial\Omega$. $A(\mathbf{r};n,n')$ is a function that denotes refractive index mismatched between tissue and the surrounding medium, which is detailed in [22].

Therefore, deriving from Eq. (2), the exiting flux density for the ϑth band on the boundary captured by a highly sensitive CCD camera is given by [22]

$$V_\vartheta(\mathbf{r}) = -D_\vartheta(\mathbf{r})(v(\mathbf{r}) \cdot \nabla\Phi_\vartheta(\mathbf{r})) = \frac{\Phi_\vartheta(\mathbf{r})}{2A(\mathbf{r};n,n')} \quad (\mathbf{r} \in \partial\Omega).$$
(3)

Based on the diffusion equation Eq. (1) and its boundary condition Eq. (2), a variational formulation is derived. Then, using the finite element method (FEM), the variational formulation is discretized by piecewise-linear finite elements [9,22]. Consequently, after a series of transformations and rearrangements, a linear relationship is constructed between source distribution inside heterogeneous medium and the boundary measurement in the ϑth band on the surface:

$$M_\vartheta q_\vartheta(\mathbf{r}) = \Phi_\vartheta.$$
(4)

Now we are ready to formulate multispectral BLT. Given the energy contribution percentage for each spectral band, which can be determined by the *a priori* experimental spectral analysis of the bioluminescent source—$q_\vartheta(\mathbf{r}) = \omega_\vartheta q(\mathbf{r})$, where $\Sigma_{\vartheta=1}^m \omega_\vartheta \approx 1$—the following equation for multispectral BLT is obtained [18,22]:

$$Mq(\mathbf{r}) = \Phi^{meas},$$
(5)

where

$$Mq(\mathbf{r}) = \begin{bmatrix} \omega_1 M_1[q(\mathbf{r})] \\ \omega_2 M_2[q(\mathbf{r})] \\ \vdots \\ \omega_m M_m[q(\mathbf{r})] \end{bmatrix}, \quad and \;\; \Phi^{meas} = \begin{bmatrix} \Phi_1 \\ \Phi_2 \\ \vdots \\ \Phi_m \end{bmatrix}.$$
(6)

Because the problem is ill-posed, the output-least-squares formulation incorporated with a regularization

term is commonly used in practice. The solution of the problem Eq. (5) can be determined by minimizing the following objective function:

$$F(q) = \frac{1}{2}\|Mq(\mathbf{r}) - \Phi^{meas}\|_2^2 + \frac{1}{2}\beta\|q(\mathbf{r})\|_2^2, \qquad (7)$$

where β is the Tikhonov regularization parameter that controls the regularity of the identified coefficient $q(\mathbf{r})$. Here $\|\cdot\|_2$ denotes the L_2 norm.

3. LEVEL-SET-BASED RECONSTRUCTION METHOD

A. Piecewise-Constant Level-Set Method for Bioluminescence Tomography

The essential ideas of the piecewise-constant level-set method will be presented in this section. Assume that the domain Ω can be partitioned into a set of subdomains $\{\Omega_i\}_{i=1}^n$. In order to identify the subdomains, we define a level-set function ϕ that governs topological changes of the bioluminescent source distribution such that [40]

$$\phi = i \quad in \ \Omega_i, \quad i = 1, 2, \cdots, n. \qquad (8)$$

Thus for any given partition $\{\Omega_i\}_{i=1}^n$, its corresponding function ϕ takes the value $1, 2, \cdots, n$. Associated with a level-set function ϕ, the characteristic functions of the subdomains are given as [41]

$$\psi_i = \frac{1}{\alpha_i}\prod_{j=1, j\neq i}^n (\phi - j), \quad where \ \alpha_i = \prod_{k=1, k\neq i}^n (i - k). \qquad (9)$$

If ϕ is given as in Eq. (8), we have $\psi_i = 1$ for $\mathbf{r} \in \Omega_i$ and $\psi_i = 0$ elsewhere. Suppose $q(\mathbf{r})$ is defined in domains $\Omega = \cup_{i=1}^n \Omega_i$, and $q(\mathbf{r}) = c_i$, $\mathbf{r} \in \Omega_i$. Here c_i denotes the strength of source on each phase. Therefore, we have the piecewise-constant function:

$$q(\mathbf{r}) = q(\phi, \mathbf{c})(\mathbf{r}) = \sum_{i=1}^n c_i\psi_i(\phi), \qquad (10)$$

where $\mathbf{c} = (c_1, c_2, \cdots, c_n)^T$. It is clear that $q = c_i$, in Ω_i. To satisfy Eq. (8), we need to impose some constraints on ϕ. We define

$$K(\phi) = \prod_{i=1}^n (\phi - i). \qquad (11)$$

Incorporating Eq. (7) with the constraints above, the BLT inverse problem becomes

$$\min_{\phi, \mathbf{c}} F(\phi, \mathbf{c}) = \min_{\phi, \mathbf{c}} F(q(\phi, \mathbf{c})), \quad subject \ to \ K(\phi) = 0. \tag{12}$$

B. Algorithm

Since BLT is an ill-posed inverse problem, the minimization scheme Eq. (7) is commonly time-consuming. By using the augmented Lagrangian strategy, the inverse problem is reduced to a coupled linear algebraic system, which can be solved efficiently [44]. The augmented strategy is a

combination of the multiplier strategy and the penalization strategy. Define it as an accessoryl function with Eq. (12) [38]:

$$L(\phi, \mathbf{c}, \lambda) = F(\phi, \mathbf{c}) + \int_\Omega \eta K(\phi)\mathrm{d}\mathbf{r} + \frac{1}{2\mu}\int_\Omega K^2(\phi)\mathrm{d}\mathbf{r}. \tag{13}$$

Now the minimization problem Eq. (12) has been transformed into the following minimization problem:

$$\min_{\phi, \mathbf{c}, \eta} L(\phi, \mathbf{c}, \eta), \qquad (14)$$

where η is the Lagrangian multiplier that is defined in the same domain and μ is a penalization parameter, which should be a positive number to enforce $K(\phi) = 0$. Note that when the constraints are fulfilled, the Lagrangian term and the penalization term will vanish, and $L = F$.

For the problem, we should solve Eq. (14), which in turn will give the solution of Eq. (12). Hence, the derivatives of L with respect to ϕ, $\mathbf{c}$, and η are needed. By the chain rule, we now have [34,35]

$$\begin{cases} \dfrac{\partial L}{\partial \phi} = \dfrac{\partial F}{\partial q}\dfrac{\partial q}{\partial \phi} + \eta K'(\phi) + \dfrac{1}{\mu}K(\phi)K'(\phi), & (15a) \\[3mm] \dfrac{\partial L}{\partial c_i} = \dfrac{\partial F}{\partial c_i} = \int_\Omega \dfrac{\partial F}{\partial q}\dfrac{\partial q}{\partial c_i}\mathrm{d}\mathbf{r} \ (i = 1, 2, \cdots, n), & (15b) \\[3mm] \dfrac{\partial L}{\partial \eta} = K(\phi), & (15c) \end{cases}$$

where

$$\begin{cases} \dfrac{\partial F}{\partial q} = (Mq)^T[Mq - \Phi^{meas}] + \beta q, & (16a) \\[3mm] \dfrac{\partial q}{\partial \phi} = \sum_{i=1}^n c_i\psi_i'(\phi), & (16b) \\[3mm] \dfrac{\partial q}{\partial c_i} = \psi_i \ (i = 1, 2, \cdots, n). & (16c) \end{cases}$$

To find the minimization point, we should use an iterative algorithm. Since we want these three derivatives Eqs. (15) to equal zero, we increase k until none of $\phi, \mathbf{c}, \eta$ changes anymore. Using this approach, we need to choose three different schemes to get $\phi^{k+1}, \mathbf{c}^{k+1}, \eta^{k+1}$ from $\phi^k, \mathbf{c}^k, \eta^k$. The updating formulas for ϕ, $\mathbf{c}$, and η are shown in the flow chart of Fig. 1.

It should be noted that the minimization with respect to ϕ is most time-consuming. We introduce an artificial time variable and solve the following partial differential equation to steady state [35]:

$$\phi_t + \frac{\partial L}{\partial \phi} = 0. \tag{17}$$

At steady state, $\phi_t = 0$ means $\partial L/\partial \phi = 0$. On behalf of getting better efficiency and stability, we use *the operator splitting scheme* [45] to solve Eq. (17): given ϕ^0, we find $\phi^{k+1/2}$ and ϕ^{k+1} from the following equations for $k = 1, 2, \ldots$:
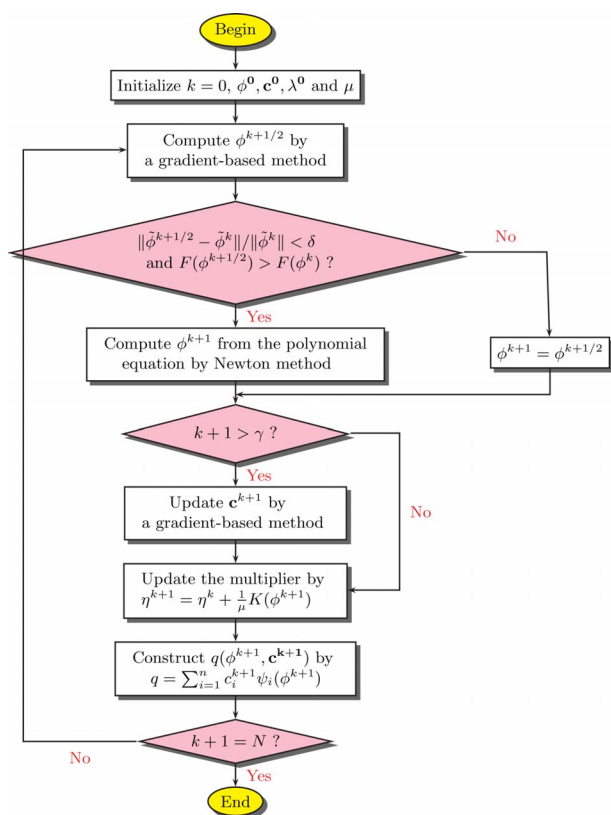
Fig. 1.   (Color online) Flowchart of the proposed method.

$$\begin{cases} \dfrac{\phi^{k+1/2} - \phi^k}{\Delta t} + \dfrac{\partial F}{\partial \phi}(\phi^k, \mathbf{c}^k, \eta^k) = 0, & \text{(18a)} \\[2mm] \dfrac{\phi^{k+1} - \phi^{k+1/2}}{\Delta t} + \eta K'(\phi^{k+1}) + \dfrac{1}{\mu}K(\phi^{k+1})K'(\phi^{k+1}) = 0, & \text{(18b)} \end{cases}$$

where Δt is an artificial time step. Equation (18a) is solved by a gradient-based method to obtain the solution for $\phi^{k+1/2}$. Equation (18b) is the constraint equation, which can be rewritten as

$$\phi^{k+1} - \phi^{k+1/2} + \Delta t\, \eta K'(\phi^{k+1}) + \tau_2 K(\phi^{k+1})K'(\phi^{k+1}) = 0,$$
(19)

where $\tau_2 = \Delta t / \mu$. We need to find the roots for this polynomial of the order $2n-1$. According to the rules in [46], by choosing the artificial time step Δt and penalization parameter μ, the equation has only one real root. The quasi-Newton method can be used to get the roots very efficiently [47].

4. EXPERIMENTS AND RESULTS

A. Numerical Experiments

1. Reconstructions with Different Initial Values and More Phases than Actually Needed
We first consider numerical cases to verify our proposed method. In this part, a heterogeneous tissue-like model was employed. This cylinder model with 30 mm height and 24 mm diameter was composed of muscle, two lungs, heart, liver, and bone, as depicted in Fig. 2(a). It was discretized into 4571 nodes and 21,998 tetrahedron ele-
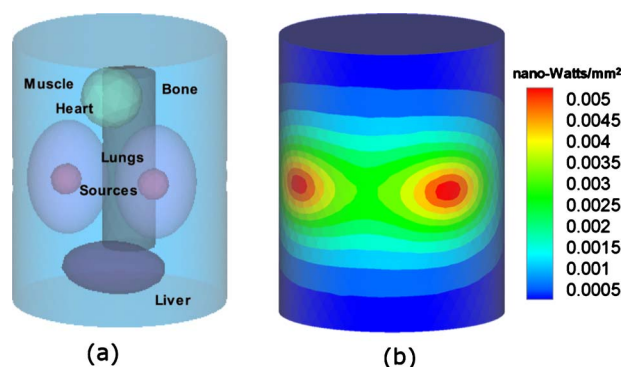

Fig. 2.   (Color online) Heterogeneous tissue-like model and associated BLI simulation measurements. (a) Tissue-like model with regions geometrically similar to heart (green online), lungs (purple online), liver (navy blue online), bone (gray), muscle (the remainder), and two sources embedded in two lungs. (b) Measured bioluminescent data of the 625–675 nm band mapped onto the finite element mesh model. The front view of the model is shown.

ments. Two sphere bioluminescent sources with 1.8 mm radius and 0.238 nW/mm^3 power density were embedded in the left and right lungs, locations $(-5, 5, 15)$ and $(-5, -5, 15)$, respectively. Furthermore, in order to reduce the number of unknown variables, the DOI was specified as $\Omega = \{(x, y, z) | x \leq -1.0, 12.0 \leq z \leq 18.0\}$. The number of elements in the DOI was about 19% of all the elements in the phantom. All the reconstructions were performed on our desktop computer with Intel Core 2 Duo 1.86 GHz CPU and 3 GB RAM.

Bioluminescent enzymes create broad emission spectra. Based on the bioluminescent spectral analysis [48], the emission spectra may be divided into three bands: [575–625 nm], [625–675 nm], and [675–725 nm] for this numerical experiment. By integrating the intensity over each band, the energy distribution percentage was quantified as $\omega_1 = 0.38$ for the first band, $\omega_2 = 0.43$ for second, and $\omega_3 = 0.19$ for third. Simulated measurement data of the exiting flux density for each band, generated by a classical finite element forward method, were captured on about 2000 nodes along the entire surface of the model (Fig. 2(b)). The optical properties for each region and band were estimated using the method in [49]. They are all summarized in Table 1.

Three cases with different initial constant values using the proposed method and one case using the quasi-Newton method were carried out. Based on the proposed method, the initial constant values for all phases, which denote the source strength, are summarized in Table 2. The number of phases was set as that actually needed, which was two in these cases. The level-set function ϕ was initially 1.50 over the entire DOI in all cases. This means that over the DOI, the initial values contain no information. Moreover, the regularization parameter β was selected as 3.0×10^{-3}, the step threshold $\gamma = 200$, the penalization parameter $\mu = 2000$, and the artificial time step $\Delta t = 0.10$. In this case, since the entire region has two phases, Eq. (19) is a third-order polynomial equation. To guarantee that the equation has only one real root, τ_2 is not larger than 2 [46]. Here we selected $\tau_2 = 0.20$. In the quasi-Newton method, the initial values on all the points

Table 1. Optical Properties for Each Region in the Heterogeneous Tissue-Like Mode[a]

	575–625 nm		625–675 nm		675–725 nm	
	μ_a	μ_s'	μ_a	μ_s'	μ_a	μ_s'
Muscle	0.0317	0.586	0.0089	0.467	0.0063	0.379
Heart	0.0218	1.129	0.0064	1.007	0.0052	0.905
Lungs	0.0707	2.305	0.0195	2.209	0.0125	2.124
Liver	0.1275	0.761	0.0329	0.700	0.0176	0.648
Bone	0.0024	2.935	0.0009	2.609	0.0011	2.340

[a]The units of both μ_a and μ_s' are mm^{-1}

Table 2. Source Strength Reconstruction Results from Surface Measurements Corrupted by 1% Gaussian Noise for Different Groups of Initial Strength[a]

	Init. Strength		Recons. Strength		Relative Error	Max. Iter. Step	Time (s)
	c_1	c_2	c_1	c_2			
LS	0.80	0.0	0.233	−0.011	2.10%	1200	585
	1.00	0.0	0.270	−0.015	13.45%	1600	813
	1.50	0.0	0.334	−0.022	40.34%	2000	987
QN	0.001		0.101		57.98%	1000	2405

[a]LS, level-set based method; QN, quasi-Newton method. The unit for source strength is nano-Watts/mm^3.

were set as shown in Table 2, and the regularization parameter was the same as above.

Additionally, in some cases, it might not be possible to reliably deterimine the number of phases *a priori*. By introducing more phases than actually needed, the proposed method can handle this problem. In this experiment, while the number of phases actually needed was two, we set it as three. The geometrical model and other parameters were the same as above. Note that although Eq. (19) is fifth order for three phases, τ_2 was the same as the cases above, which can also guarantee that this equation has only one real root [46].
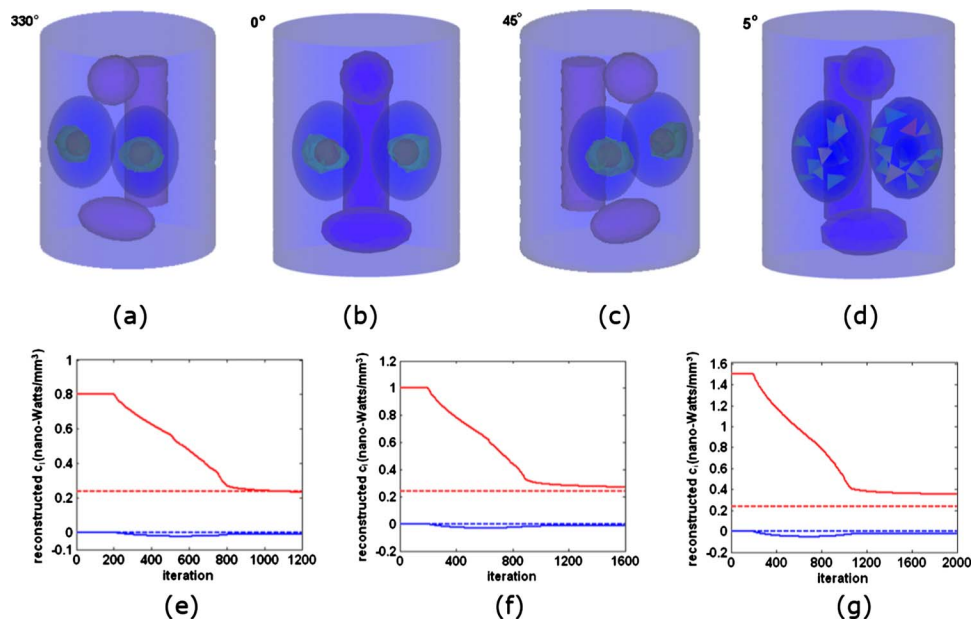

Fig. 3. (Color online) BLT reconstructions of two bioluminescent sources in the heterogeneous experiments from BLI measurements corrupted by 1.0% Gaussian noise using both the proposed method and the quasi-Newton method. Three-dimensional locations are shown of reconstructed results (green online) and actual results (red online) in two lungs with the proposed method for (a) initial strength 0.8, 0.0 nW/mm^3, (b) 1.0, 0.0 nW/mm^3, and (c) 1.5, 0.0 nW/mm^3 for each each phase. (d) Reconstruction results based on the quasi-Newton method with 1.0% Gaussian noise. (e), (f), and (g) Source strength c_i $(i=1,2)$ evolution during reconstructions as a function of iteration associated with (a), (b), and (c), respectively. Reconstructed c_1 is shown as the upper (red online) solid line, reconstructed c_2 as the lower (blue online) solid line. Actual c_1 and c_2 are shown as upper and lower (red and blue online) dashed lines, respectively. The angle at the upper left of (a)–(d) represents the rotating angle of the model from the front view; the angle increases in the counterclockwise direction.
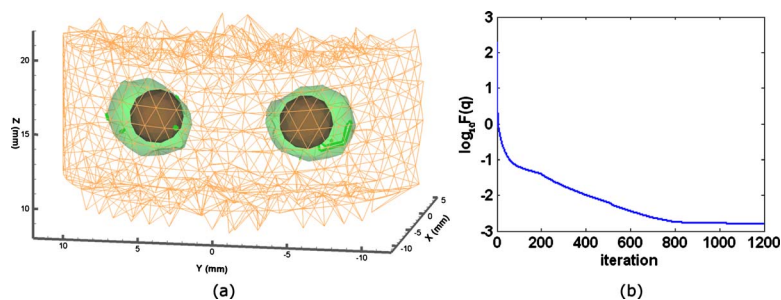
Fig. 4.   (Color online) Local amplification of the reconstructed sources and its convergence curve. (a) Results with 1% Gaussian noise and initial strength 0.8, 0.0 nW/mm^3. (b) Logarithm of $F(q)$ with 10 as a function of iteration step for the case of initial strength 0.8, 0.0 nW/mm^3.

Figures 3(a)–3(c) depict the reconstructed locations for two sources given three groups of different initial source strength respectively, and Fig. 3(d) shows the results of the quasi-Newton method. It is noted that Fig. 3(b) shows the experiment with three phases. Since the case with two phases are very similar to it, we omit it. Figure 4(b) is the local amplification for the results in Fig. 3(a). As anticipated, the reconstructed sources reliably localized the real ones. As seen in Fig. 3(b), the redundant regions merged with the other regions during the iterative process, and the reliable results can also be reconstructed. While the proposed method can work well with such large DOI, the quasi-Newton method cannot. As shown in Fig. 3(d), many small pieces distribute widely in lungs, and one cannot determine the location of the real sources. The results based on the quasi-Newton method may become reliable until the elements in DOI constitute less than 4% of all the elements, as in [9,10,16,17,20].

Quantitatively, the associated source strength evolutions during the whole reconstructions are shown in Fig. 3(e)–3(g), which indicate that the strength for each phase approaches to the real ones with increasing iteration steps. However, in the quasi-Newton method, the relative error of the source strength is much higher. A detailed comparison between the proposed method and the quasi-Newton method is listed in Table 2. It is shown that the quasi-Newton method requires much more time than the proposed method does, and its results are less reliable than those of the proposed method.

Furthermore, during the reconstructions for the case of initial strength 0.8, 0.0 nW/mm^3, as shown in Fig. 4(b), the object function $F(q)$ is almost monotonically decreasing, which clearly shows the evolution is convergent. Because the curves for other cases are similar to this one, we omit them for brevity. The set of results indicates that
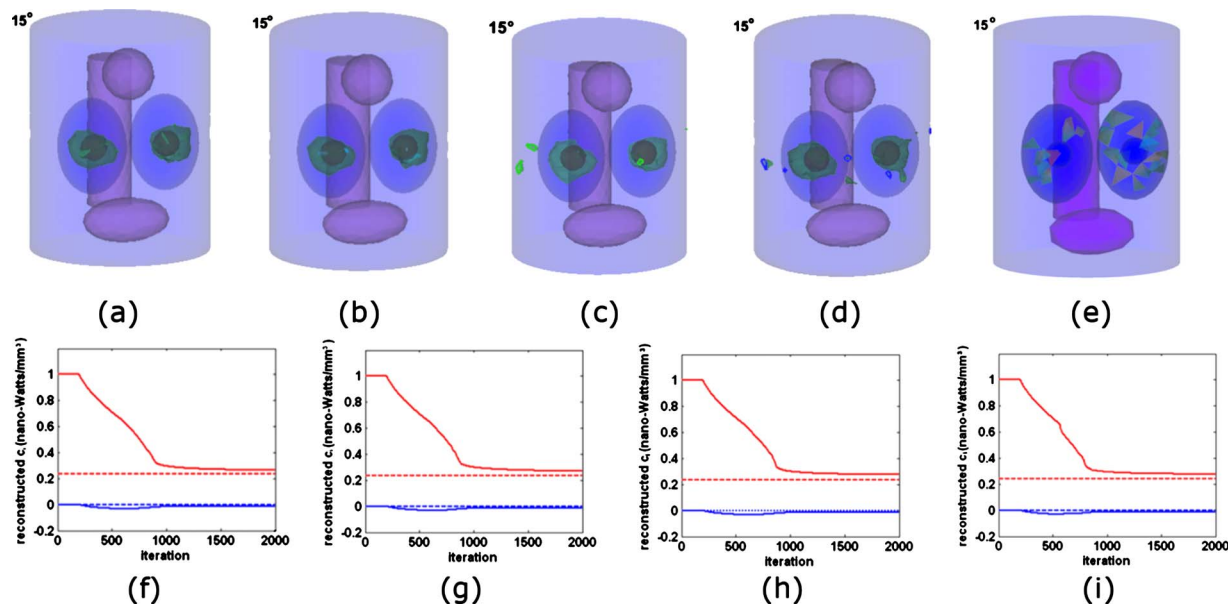

Fig. 5.   (Color online) BLT reconstructions in the heterogeneous experiments from BLI measurements corrupted by different Gaussian noise levels. three-dimensional level-set reconstructions of the location of sources (green online) and actual sources (red online) in two lungs for (a) 0.25% Gaussian noise, (b) 6.25% Gaussian noise, (c) 10% Gaussian noise, and (d) 25% Gaussian noise. (e) Reconstruction results based on the quasi-Newton method with 25% Gaussian noise. (f), (g), (h), and (i) Source strength c_i $(i=1,2)$ evolution during reconstructions as a function of iteration step associated with (a), (b), (c), and (d), respectively. Reconstructed c_1 is shown as upper (red online) solid line, reconstructed c_2 as lower (blue online) solid line. Actual c_1 and c_2 are shown as upper and lower (red and blue online) dashed lines, respectively.

Table 3. Reconstruction Results from Surface Measurements Corrupted by Different Gaussian Noise Levels[a]

	Noise Level	SNR Level (dB)	Recons. Strength		Relative Error	Time (s)
			c_1	c_2		
LS	0.25%	26.02	0.264	−0.014	11.09%	964
	1.00%	20.00	0.267	−0.014	12.18%	987
	6.25%	12.04	0.271	−0.014	13.87%	1012
	10.00%	10.00	0.276	−0.015	15.97%	999
	25.00%	6.02	0.277	−0.014	16.39%	981
QN	25.00%	6.02	0.09		62.18%	2387

[a]The unit for source strength is nano-Watts/mm^3.

$F(q)$ approaches zero with different cases of initial strength.

2. Reconstructions with Different Noise Levels
In order to evaluate the sensitivity of the proposed method to various noise levels, five cases using measurements corrupted by 0.25%, 1.00%, 6.25%, 10.00%, and 25.00% Gaussian noise were carried out, and the quasi-Newton method with 25.00% Gaussian noise was compared with them. The geometry model and the optical properties were the same as in the previous subsection, as presented in Fig. 2(a). The initial strength for the two phases was 1.0 and 0.0 nW/mm^3, respectively, and other parameters were same as mentioned above. All the parameters of the quasi-Newton method were the same as those in Subsection 4.A.1.

Figures 5, 3(b), and 3(f) demonstrate the tolerance of the proposed method for noise levels. As shown in Fig. 5(a)–5(c) and Fig. 3(b), the locations are feasibly recovered. Here, the results of 1.0% noise in Fig. 3(b) and 3(f) are very similar to those of 2000 iteration steps, so they are not repeated in Fig. 5. Even using the BLI measurement data corrupted by 25% noise, the bioluminescent sources can still be reasonably located and quantified, and the relative error was about 16.39%, as shown in Fig. 5(d) and 5(i). Because of high noise, we can find some very small regions spreading around the sources, but the real results can be obviously determined. However, the quasi-Newton method cannot reliably recover the source with 25% noise, as depicted in Fig. 5(e). The relative error of the source strength is much higher than that of the proposed methods as listed in Table 3. It is only when the DOI is diminished and noise is reduced that one may get reliable results using the quasi-Newton method, similar to the results in [9,16].

Quantitatively, the strength of the sources can also be properly quantified in all noise levels (Figs. 5(f)–5(i) and Fig. 3(f)). In Fig. 6, it is observed that the relative error of the strength correlates well with the signal-to-noise ratio (SNR) levels. It clearly suggests that this method is insensitive to noise.

Furthermore, the run time for all cases was about 1000 s with little variation. By contrast, the process based on the quasi-Newton method requires about 2400 s. Note that the run time is strongly influenced by the model's degree of refinement. A finer model produces recovered results that better resemble the real ones, so we

should try to maintain a balance between run time and recovered accuracy to achieve the best efficiency. A detailed comparison of the results of the proposed method and the quasi-Newton method is presented in Table 3.

3. Mouse Atlas Verification
Numerical results using a mouse atlas are presented here to verify the performance of the proposed method for mouse applications. First, an atlas of the BALB/c mouse was developed utilizing our micro-CT system and cone-beam reconstruction algorithm, as shown in Fig. 7(a) [50,51]. By using image processing and interactive segmentation methods, some primary organs, including heart, lung, liver, bone, and muscle, were delineated, and the optical coefficients for each organ were the same as those in the cylinder phantom (Table 1). Then the mouse atlas was discreted into volumetric mesh. This discreted mesh contains 4614 nodes and 25,783 tetrahedral elements. The real source was located at about the center of atlas, at a depth of about 7 mm from the surface, with coordinates (21.45, 33.65, 14.52) in liver, diameter of 1.48 mm, and source strength of 0.238 nW/mm^3. The DOI was specified as $\Omega = \{(x,y,z) \mid 25.0 \leq y \leq 35.0, 10.0 \leq z \leq 18.0\}$, and the elements in the DOI were about 25% of the mouse atlas. The parameters in the algorithm, the three spectral bands, and the corresponding energy distribution percentage were the same as in the cases of the two phases in Subsection 4.A.1. The initial source strength for each phase was set as 2.0 and 0.0 nW/mm^3.

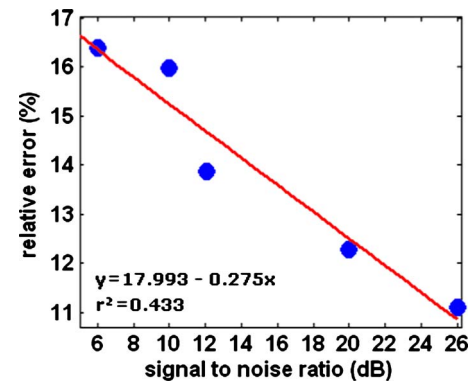$$y = 17.993 - 0.275x$$
$$r^2 = 0.433$$

Fig. 6. (Color online) Linear regression with different noise levels. The solid line denotes the linear regression, and the solid points represent the reconstructed results.

The reconstruction results in Fig. 7 demonstrate the effectiveness of the proposed method in the heterogeneous mouse atlas. As depicted in Fig. 7(a), the source was feasibly localized. Figure 7(b) shows the evolution process and the final values for the source strength. The reconstructed source strength was 0.194 nW/mm^3, with relative error of 18.49%. As anticipated, the object function $F(q)$ decreases with increase in the iteration steps, and the final results are obtained when the decrement is nearly negligible. This reconstruction went through about 800 steps at a time cost of 798 s.

B. Physical Experiment

1. Experimental System Setup and Calibration

A physical heterogeneous experiment was implemented to demonstrate further the feasibility of the proposed method. Our optical imaging system was utilized for data acquisition. The detector is made using a highly sensitive CCD camera (VersArray 1300B, Princeton Instruments, Trenton, New Jersey, USA) coupled to a lens (Nikkor 17−55 mm f/2.8G, Nikon, Japan) and utilizing 1340 ×1300 pixels (20 μm×20 μm size) with 16-bit dynamic-range images. This detector coupled with different spec-
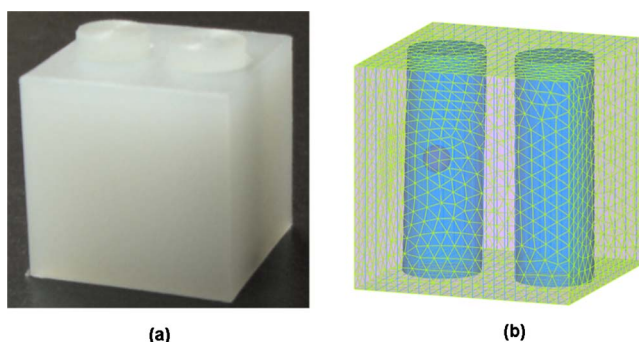

(a)   **(b)**

Fig. 8. (Color online) Physical heterogeneous phantom. (a) Profile of the physical phantom. (b) Mesh with regions similar to lungs (the two blue cylinders), source (the red sphere in the cylinder on the left), and muscle (the remaining part).

tral filters is calibrated by an integrating sphere (USS-1200V-LL Low-Light Uniform Source, Labsphere, North Sutton, New Hampshire, USA). The range of source power used in the calibration is $\sim$0.0014−0.0432 nW/mm^2. For the multispectral range of interest and exposure time of 15 s, the calibration formulas for the CCD camera are given by

$$\begin{cases} V_1 = 2.3302 \times 10^{-6} \cdot value + 5.5093 \times 10^{-4} \; in[600-650 \text{ nm}], & (20a) \\ V_2 = 2.0859 \times 10^{-6} \cdot value + 4.2666 \times 10^{-4} \; in[650-700 \text{ nm}], & (20b) \\ V_3 = 1.9477 \times 10^{-6} \cdot value + 1.3464 \times 10^{-4} \; in[700-760 \text{ nm}], & (20c) \end{cases}$$

where V_ϑ (nW/mm^2) denotes the exiting flux density and *value* the gray value on each pixel for $\vartheta=1,2,3$. Before data acquisition, the CCD was cooled to −110 °C using liquid nitrogen to reduce dark noise. During acquisition, a heterogeneous phantom was controlled by a rotation stage (RAK 100, Zolix Instruments, Beijing, China), and images were captured by the camera around this phantom for every 90°.

2. Phantom and Optical Parameters

In this experiment, a cube heterogeneous phantom with 20 mm side length was designed and manufactured as depicted in Fig. 8. In the phantom, two tissue-like parts, which denote muscle and two lungs, were made of polyethylene and polypropylene respectively, and one sphere of 2.5 mm diameter was machined in the phantom with the center at (4,10,10.5). The bioluminescent source in the phantom was simulated by luminescent chemical reaction from a luminescent light stick. The compounds were extracted from the stick and injected into the hole. After thorough mixing, a red light whose emission wavelength ranged between about 600 nm and 760 nm was emitted due to the chemical reaction of the mixed resolutions, and the energy distribution percentage in three spectrum bands, which was measured by a spectrometer, was 0.54 for [600−650 nm], 0.36 for [650−700 nm] and 0.10 for [700−760 nm]. The source strength was $\sim$22.69 nW/mm^3. In addition, the optical parameters of the phantom were determined by a time-correlated single photon counting (TCSPC) system specifically [52]. The
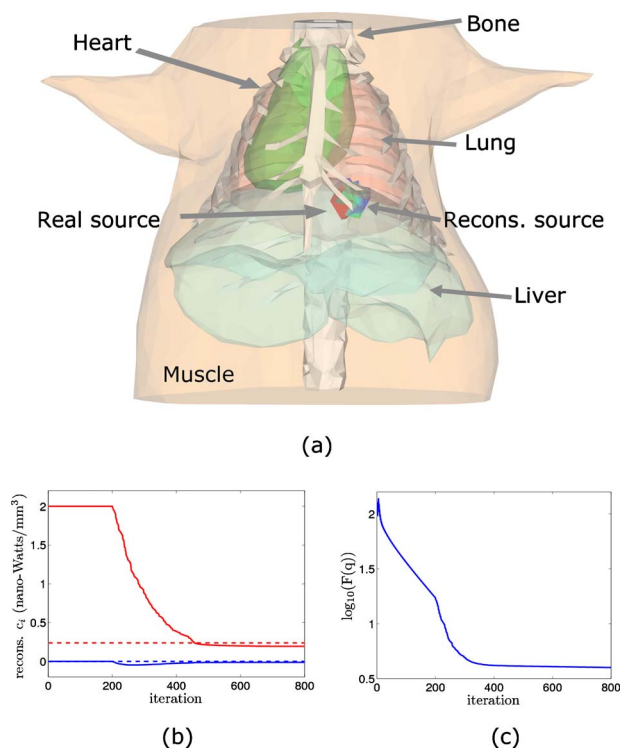

(a)

(b)   **(c)**

Fig. 7. (Color online) BLT reconstructions in the heterogeneous mouse atlas. (a) Reconstructed location in three dimensions. (b) Source strength evolution during reconstructions as a function of iteration step. (c) Logarithm of $F(q)$ with 10 as a function of iteration step.

Table 4. Optical Parameters for Each Region in the Heterogeneous Phantom[a]

	600−650 nm		650−700 nm		700−760 nm	
	μ_a	μ_s'	μ_a	μ_s'	μ_a	μ_s'
Muscle	0.000041	0.141	0.00002	0.1770	0.0028	0.3181
Lungs	0.003	0.170	0.001	0.2361	0.0034	0.3540

[a]The units of both μ_a and μ_s' are mm^{-1}.

measured optical parameters for each region of the phantom for three spectrum bands are listed in Table 4.

3. BLI Data Acquisition and Data Processing

BLI data were acquired in an ideally dark environment. In each spectrum band, the images on four side faces of the phantom were taken with exposure time of 15 s. Afterward, the pixel gray values on each view were transformed into corresponding light units according to the above-mentioned calibration relationship for the three spectrum bands.

4. Bioluminescent Source Reconstructions

The cube phantom used in reconstruction was discretized into 3402 nodes and 14,165 elements, and 1377 nodes on the surface as presented. The exiting flux density Φ_ϑ on the ϑth band was obtained from the BLI data V_ϑ in light units, where $\vartheta = 1, 2, 3$. Finally, we used the proposed method to recover the source distribution in the heterogeneous model. In this part, the initial strength for the two phases was 500.0 and 0.0 nW/mm^3 , and the regularization parameter was set as 8.0×10^{-4}. The level-set function ϕ was initially 1.50 over the entire DOI, and other

(a)   (b)
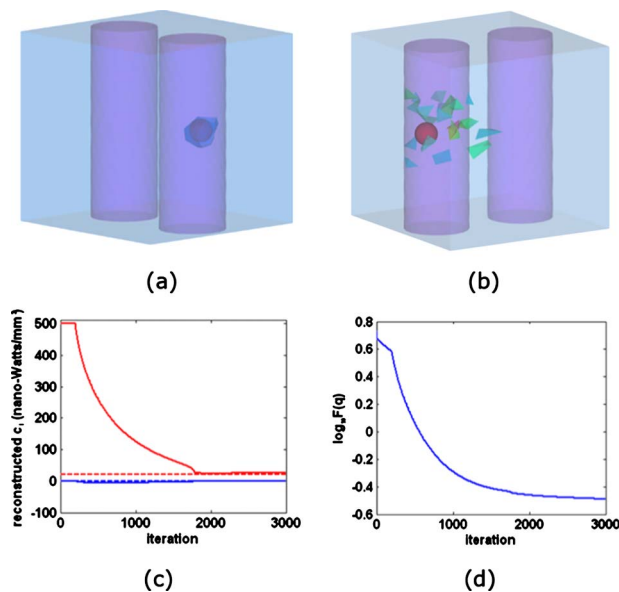

(c)   (d)

Fig. 9. (Color online) BLT reconstructions in the physical experiment. (a) Three-dimensional level-set reconstructions of the location of source (blue online) and actual source (red online) in the phantom. (b) Reconstruction results based on the quasi-Newton method. (c) Source strength c_i $(i = 1, 2)$ evolution during reconstructions as a function of iteration. Reconstructed c_1 and c_2 are drawn as upper and lower (red and blue online) solid lines, respectively, actual c_1 and c_2 in upper and lower (red and blue online) dashed lines, respectively. (d) Logarithm of $F(q)$ with 10 as a function of iteration step.

parameters were the same as in Subsection 4.A. Additionally, in order to reduce the number of unknown variables, the DOI Ω was specified as $\{(x,y,z)|(x-5)^2+(y-10)^2 \leqslant 16, 7.5 \leqslant z \leqslant 14.5\}$. For the quasi-Newton method, approximately the best regularization parameter was selected as 3.0×10^{-3}.

The reconstruction results of the proposed method are demonstrated in Fig. 9(a). The recovered location matches the real one reliably. Furthermore, as the evolution curves in Fig. 9(c) illustrate, the strength of the source evolves with increase in the number of iteration steps and gradually approaches the real source density. In the end, the recovered strength of the source is 24.87 nW/mm^3, with a relative error of 9.61%. Consistent with the results of numerical experiments in Subsection 4.A, the evolution process is stable, as shown in Fig. 9(d), and the object function $F(q)$ is almost monotonically decreasing. In this case, the time cost for reconstruction was about 150 s. By contrast, the results based on the quasi-Newton method spread over a relative large region and do not recover the source properly, as shown in Fig. 9(b). Quantitatively, the reconstructed strength is sensitive to the initial values. In this case, for the initial value of 1.0 nW/mm^3, the average of the source strength is 9.2 nW/mm^3, and the relative error is 59.45%. With decreasing DOI, the performance of the quasi-Newton method will improve, which is consistent with the results of the quasi-Newton method discussed in Subsection 4.A. The time cost is about 490 s.

5. CONCLUSION

We have developed a method based on a level-set strategy to reconstruct bioluminescent sources in three dimensions from measured multispectral data. In the piecewise-constant level-set approach, while the level-set function is to localize sources, the constant value in each phase is to recover the source strength. Furthermore, because each spectral measurement may be viewed as adding some amount of independent information to the inverse problem, multispectral measurements are utilized as *a priori* information to reduce the ill-posedness of BLT. Both numerical and physical experiments demonstrate the effectiveness and efficiency of this proposed method.

In numerical experiments, the heterogeneous reconstructions using a phantom clearly demonstrate that the proposed method is reliable and fairly robust with respect to various conditions, such as initial values and high noise levels. Furthermore, it can still work when the number of phases is not known *a priori*, which may happen in some applications [39]. Compared with other methods [9,10,16,17,20], this method can get reliable results on larger DOI. A mouse atlas reconstruction was presented

to demonstrate the effectiveness of the proposed method in turbid mouse geometry. The physical experiment further evaluates its potential in practical applications.

While we believe that some errors in the physical experiment have been revised or optimized to some degree, in future experiments we will further analyze systemically and quantitatively the relation between precision of the system and measurement bias, optical filters, and inaccuracy of optical characteristics, as well as further optimize the imaging system.

In conclusion, we have developed a level-set-based reconstruction method for spectrally resolved three-dimensional BLT and demonstrated its feasibility and efficiency for recovering the features of bioluminescent sources in various experimental, even rigorous, conditions. *In vivo* mouse studies based on level set and comprehensive error analysis of the imaging system will be reported in the future.

ACKNOWLEDGMENTS

[†]Contributed equally to this work.

REFERENCES

1. H. Herschman, "Molecular imaging: looking at problems, seeing solutions," Science **302**, 605–608 (2003).
2. V. Ntziachristos, J. Ripoll, L. V. Wang, and R. Weisslder, "Looking and listening to light: the evolution of whole body photonic imaging," Nat. Biotechnol. **23**, 313–320 (2005).
3. R. Weissleder and M. J. Pittet, "Imaging in the era of molecular oncology," Nature **452**, 580–589 (2008).
4. J. K. Willmann, N. van Bruggen, L. M. Dinkelborg, and S. S. Gambhir, "Molecular imaging in drug development," Nat. Rev. Drug Discovery **7**, 591–607 (2008).
5. J. Tian, J. Bai, X.-P. Yan, S.-L. Bao, Y.-H. Li, W. Liang, and X. Yang, "Multimodality molecular imaging," IEEE Eng. Med. Biol. Mag. **27**, 48–57 (2008).
6. R. Weissleder and V. Ntziachristos, "Shedding light onto live molecular targets," Nat. Med. **9**, 123–128 (2003).
7. G. Wang, E. A. Hoffman, G. McLennan, L. V. Wang, M. Suter, and J. F. Meinel, "Development of the first bioluminescence CT scanner," Radiology **229**, 566 (2003).
8. X. Gu, Q. Zhang, L. Larcom, and H.-B. Jiang, "three-dimensional bioluminescence tomography with model based reconstruction," Opt. Express **12**, 3996–4000 (2004).
9. W.-X. Cong, G. Wang, D. Kumar, Y. Liu, M. Jiang, L. V. Wang, E. Hoffman, G. McLennan, P. McCray, J. Zabner, and A. Cong, "Practical reconstruction method for bioluminescence tomography," Opt. Express **13**, 6756–6771 (2005).
10. W.-X. Cong and G. Wang, "Boundary integral method for bioluminescence tomography," J. Biomed. Opt. **11**, 020503 (2006).
11. N. V. Slavine, M. A. Lewis, E. Richer, and P. P. Antich, "Iterative reconstruction method for light emitting sources based on the diffusion equation," Med. Phys. **33**, 61–68 (2006).
12. Y.-J. Lu, A. Douraghy, H. B. Machado, D. Stout, J. Tian, H. Herschman, and A. F. Chatziioannou, "Spectrally-resolved bioluminescence tomography with the third-order simplified spherical harmonics approximation," Phys. Med. Biol. **59**, 6477–6493 (2009).
13. J.-C. Feng, K.-B. Jia, C.-H. Qin, G.-R. Yan, S.-P. Zhu, X. Zhang, J.-T. Liu, and J. Tian, "Three-dimensional bioluminescence tomography based on Bayesian approach," Opt. Express **17**, 16834–16848 (2009).
14. A. H. Hielscher, "Optical tomographic imaging of small animals," Curr. Opin. Biotechnol. **16**, 79–88 (2005).
15. G. Wang, Y. Li, and M. Jiang, "Uniqueness theorems in bioluminescence tomography," Med. Phys. **31**, 2289–2299 (2004).
16. W.-X. Cong, D. Kumar, L. V. Wang, and G. Wang, "A Born-type approximation method for bioluminescence tomography," Med. Phys. **33**, 679–686 (2006).
17. Y.-J. Lv, J. Tian, G. Wang, W.-X. Cong, J. Luo, W. Yang, and H. Li, "A multilevel adaptive finite element algorithm for bioluminescence tomography," Opt. Express **14**, 8211–8223 (2006).
18. H. Dehghani, S. C. Davis, S. Jiang, B. W. Pogue, K. D. Paulsen, and M. S. Patterson, "Spectrally resolved bioluminescence optical tomography," Opt. Lett. **31**, 365–367 (2006).
19. A. J. Chaudhari, F. Darvas, J. R. Bading, R. A. Moats, P. S. Conti, D. J. Smith, S. R. Cherry, and R. M. Leahy, "Hyperspectral and multispectral bioluminescence optical tomography for small animal imaging," Phys. Med. Biol. **50**, 5421–5441 (2005).
20. Y.-J. Lv, J. Tian, W.-X. Cong, G. Wang, W. Yang, C.-H. Qin, and M. Xu, "Spectrally resolved bioluminescence tomography with adaptive finite element: methodology and simulation," Phys. Med. Biol. **52**, 1–16 (2007).
21. C. Kuo, O. Coquoz, T. L. Troy, H. Xu, and B. W. Rice, "Three-dimensional reconstruction of in vivo bioluminescent sources based on multispectral imaging," J. Biomed. Opt. **12**, 024007 (2007).
22. G. Wang, H.-O. Shen, W.-X. Cong, S. Zhao, and G.-W. Wei, "Temperature-modulated bioluminescence tomography," Opt. Express **14**, 7852–7871 (2006).
23. H. Gao and H.-K. Zhao, "Multilevel bioluminescence tomography based on radiative transfer equation. Part 2: total variation and l_1 data fidelity," Opt. Express **18**, 2894–2912 (2010).
24. K. Liu, J. Tian, X. Yang, Y.-J. Lu, C.-H. Qin, S.-P. Zhu, and X. Zhang, "A fast bioluminescent source localization method based on generalized graph cuts with mouse model validations," Opt. Express **18**, 3732–3745 (2010).
25. S. Osher and J. A. Sethian, "Fronts propagating with curvature dependent speed: Algorithms based on Hamilton-Jacobi formulations," J. Comput. Phys. **79**, 12–49 (1988).
26. T. F. Chan and L. Vese, "An active contour model without edges," IEEE Trans. Image Process. **10**, 266–277 (2001).
27. L. Zöllei, A. Yezzi, and T. Kapur, "A variational framework for joint segmentation and registration," in *IEEE Workshop on Mathematical Methods in Biomedical Image Analysis* (IEEE Computer Society, 2001), pp. 44–51.
28. E. T. Chung, T. F. Chan, and X.-C. Tai, "Electrical impedance tomography using level-set representation and total variational regularization," J. Comput. Phys. **205**, 357–372 (2005).
29. M. Schweiger, S. R. Arridge, O. Dorn, A. Zacharopoulos, and V. Kolehmainen, "Reconstructing absorption and diffusion shape profiles in optical tomography by a level-set technique," Opt. Lett. **31**, 471–473 (2006).
30. O. Dorn, E. Miller, and C. Rappaport, "A shape reconstruction method for electromagnetic tomography using adjoint fields and level sets," Inverse Probl. **16**, 1119–1156 (2000).

31. D. Adalsteinsson and J. A. Sethian, "A fast level-set method for propagating interfaces," J. Comput. Phys. **118**, 269–277 (1995).
32. C-W. Shu and S. Osher, "Efficient implementation of essentially non-oscillatory shock capturing schemes," J. Comput. Phys. **83**, 439–471 (1988).
33. X-D. Liu, S. Osher, and T. Chan, "Weighted essentially non-oscillatory schemes," J. Comput. Phys. **115**, 200–212 (1994).
34. S. Osher and R. P. Fedkiw, *Level Sets Methods and Dynamic Implicit Surfaces* (Springer, 2003).
35. J. Lie, M. Lysaker, and X.-C. Tai, "A binary level-set model and some applications to Mumford–Shah image segmentation," IEEE Trans. Image Process. **15**, 1171–1181 (2006).
36. O. Dorn and D. Lesselier, "Level-set methods for inverse scattering," Inverse Probl. **22**, R67–R131 (2006).
37. J. Lie, M. Lysaker, and X.-C. Tai, "A variant of the level-set method and applications to image segmentation," Math. Comput. **75**, 1155–1174 (2006).
38. A. Losnegård, O. Christiansen, and X.-C. Tai, "Piecewise-constant level-set method for 3D image segmentation," in *Scale Space and Variational Methods in Computer Vision*, F. Sgallari, A. Murli, and N. Paragios, eds. (Springer-Verlag, 2007), pp. 687–696.
39. L. A. Vese and T. F. Chan, "A multiphase level-set framework for image segmentation using the Mumford and Shah model," Int. J. Comput. Vis. **50**, 271–293 (2002).
40. X.-C. Tai, and H.-W. Li, "A piecewise-constant level-set method for elliptic inverse problems," Appl. Numer. Math. **57**, 686–696 (2007).
41. H.-W. Li, X.-C. Tai, and S. I. Aanonsen, "Reservoir description by using a piecewise-constant level-set method," J. Comput. Phys. **26**, 365–377 (2008).
42. L. V. Wang and H. Wu, *Biomedical Optics* (Wiley-Interscience, (2007).
43. C.-H. Qin, J. Tian, X. Yang, K. Liu, G.-R. Yan, J.-C. Feng, Y.-J. Lv, and M. Xu, "Galerkin-based meshless methods for photon transport in the biological tissue," Opt. Express **16**, 20317–20333 (2008).
44. T. F. Chan and X.-C. Tai, "Augmented Lagrangian and total variation methods for recovering discontinuous coefficients from elliptic equations," in *Proceedings of Computational Science for the 21st Century*, M. Bristeau, G. Etgen, W. Fitzgibbon, J. L. Lions, J. Periaux, and M. F. Wheeler, eds. (Wiley, 1997), pp. 597–607.
45. T. Lu, P. Neittaanmäki, and X.-C. Tai, "A parallel splitting up method and its application to Navier–Stokes equations," Appl. Math. Lett. **4**, 25–29 (1991).
46. O. Christiansen and X.-C. Tai, "Fast implementation of piecewise-constant level-set methods," in *Proceedings of Image Processing Based on Partial Differential Equations*, X.-C. Tai, K.-A. Lie, T. F. Chan, and S. Osher, eds. (Springer, 2007), pp. 289–308.
47. R. L. Burden and J. D. Faires, *Numerical Analysis* (Wadsworth, 2004).
48. H. Zhao, T. C. Doyle, O. Coquoz, F. Kalish, B. W. Rice, and C. H. Contag, "Emission spectra of bioluminescent reporters and interaction with mammalian tissue determine the sensitivity of detection in vivo," J. Biomed. Opt. **10**, 041210 (2005).
49. G. Alexandrakis, F. R. Rannou, and A. F. Chatziioannou, "Tomographic bioluminescence imaging by use of a combined optical-PET (OPET) system: a computer simulation feasibility study," Phys. Med. Biol. **50**, 4225–4241 (2005).
50. S.-P. Zhu, J. Tian, G.-R. Yan, C.-H. Qin, and J.-C. Feng, "Cone beam micro-CT system for small animal imaging and performance evaluation," Int. J. Biomed. Imaging **2009**, Article ID 960573 (2009). http://www.hindawi.com/journals/ijbi/2009/960573/html.
51. G.-R. Yan, J. Tian, S.-P. Zhu, Y.-K. Dai, and C.-H. Qin, "Fast cone-beam CT image reconstruction using GPU hardware," J. X-Ray Sci. Technol. **16**, 225–234 (2008).
52. H-J. Zhao, Fe. Gao, Y. Tanikawa, and Y. Yamada, "Time-resolved diffuse optical tomography and its application to in vitro and in vivo imaging," J. Biomed. Opt. **12**, 062107 (2007).